Geomechanics and Engineering, *Vol. 26, No. 2 (2021) 175-190*
https://doi.org/10.12989/gae.2021.26.2.175

Three-dimensional modeling of monopiles in sand subjected to lateral loading under static and cyclic conditions

Amin Barari*[1], Xiangwu Zeng[2], Mohammad Rezania[3] and Lars Bo Ibsen[1]

[1]*Department of the Built Environment, Aalborg University, Thomas Manns Vej 23, 9220 Aalborg Ø, Denmark*
[2]*Stevens Institute of Technology, Hoboken, New Jersey, 07030, U.S.A.*
[3]*Computational Mechanics, Civil Research Group, School of Engineering, University of Warwick, Coventry CV4 7AL, U.K.*

(Received January 15, 2021, Revised June 17, 2021, Accepted July 3, 2021)

Abstract. Here, the results of a three-dimensional finite element study of the complex interaction of horizontal and moment loads (HM) on offshore monopiles as failure envelope, are reported. A new design criterion is described which is based on critical length, ultimate limit states, load characteristics and Eigen-frequency to ensure stable behavior of laterally loaded monopiles. Numerical analyses were performed to examine nonlinear interaction of a soil-pile system for 10,000 load cycles. The resulting framework can predict angular rotation due to cyclic loading. According to the loading level and duration of a load, elastic strains accumulate in the vicinity of a pile. Fairly intermediate two-way cyclic loading induced the largest rotations irrespective of the analysis performed (i.e., drained versus partially drained). Based on the regression coefficients of the non-dimensional frameworks used, accumulating rocking deformations of a pile at seabed level appear to be dependent on cyclic load ratio, drainage condition, and duration of loading. For safe design, sensitivity of the natural frequency of offshore wind turbine (OWT) at a monopile critical length as well as shorter lengths were also examined. The analytical model proposed here for determining the natural frequency of an OWT considers that soil-structure interaction (SSI) can be represented by monopile head springs characterized by lateral stiffness, K_L, rotational stiffness, K_R, cross-coupling stiffness, K_{LR}, and parabolic soil stiffness variation with depth.

Keywords: accumulated strains; bearing strength envelopes; monopile; natural frequency

1. Introduction

Offshore wind energy currently offers the most competitive production prices among renewable energy sources. The most commonly used foundation type for offshore wind turbines (OWTs) are monopiles, which are single, open-ended steel pipe piles with diameters ≥ 4 m. These support structures currently account for > 75% of existing turbine foundations (Doherty and Gavin 2012), despite the development of other novel foundations (see Fig. 1). In the United Kingdom, the majority of operational offshore wind power plants employ monopiles at depths of up to 35 m for their support. These power plants represent the first two stages of the offshore wind energy strategy employed by the United Kingdom.

Due to the high costs of fabrication, installation, and transportation of offshore wind farms, and in order to meet future energy challenges, the potential for placing wind turbine generators with longer blades and towers in deeper waters has been considered in order to achieve greater production. However, in deeper waters, the span between a turbine's superstructure and the seabed is greater. This difference, coupled with the complex distribution of extreme environmental loading from higher load levels due to wind and waves, may threaten the serviceability limits of OWTs in deeper water. Thus, it is important that new designs safeguard offshore foundations against environmental threats. These threats include the following considerations:

- *Installation Operation*: defined as the offshore operation that is responsible for checking whether a foundation can be installed (Madsen *et al*. 2015) and for lifting the foundation from a storage position on a transport vessel for installation.
- *Ultimate Limit State (ULS)*: The maximum allowable loads on foundations that arise from all possible load scenarios are compared with bearing strength envelopes to obtain the capacity of a foundation (i.e., predominantly vertical load, lateral load, and overturning moment) (Yang *et al*. 2018, Wang *et al*. 2018, Larsen *et al*. 2013, Ibsen *et al*. 2012 and 2015, Barari and Ibsen 2019).
- *Fatigue Limit State (FLS), Serviceability Limit State (SLS) and seismic design consideration*: When designing OWTs for long-term performance, potential uncertainties in conditions need to be predicted (Lopez-Querol *et al*. 2017). For example, intensely cyclic horizontal loads can arise due to wind and wave actions. The amplitudes of these loads can be further increased by storms, earthquakes, or millions of low to intermediate amplitudes in the FLS.
- *Target Natural Frequency (Eigen frequency)*: In modern OWT systems, excitation from the rotor (i.e.,

*Corresponding author, Associate Professor
E-mail: abar@build.aau.dk

ISSN: 2005-307X (Print), 2092-6219 (Online)

1p) has a frequency range of 0.1-0.3 Hz. In addition, the frequency of the blades passing, due to the shadow generated when the blade passes the tower, induces dynamic loads to a foundation. In a representative power spectral density plot presented in Fig. 2, it is observed that the rotor frequency for a 3 MW wind turbine operationally varies from ~ 8.4-18.6 rpm, with the excitation frequency ranging from ~ 0.14-0.31 Hz (Lopez-Querol *et al*. 2017). Similarly, the typical frequency range for ocean waves varies from 0.05–0.5 Hz (Bisoi and Haldar 2014).

However, cyclic loads have been shown to act on surrounding soil and affect its properties (Barari and Ibsen 2017, Adhikari and Bhattacharya 2011). For example, these changes can potentially alter the stiffness and natural frequency of a foundation system. As a result, a shift from a design or target frequency to a value closer to forcing excitation frequencies can occur. This temporary problematic condition [particularly for soft-stiff designs in which the natural frequency of the system ranges between the lower bound (1P) and the upper bound (3P)] has been termed, "unplanned resonance", and this will significantly shorten the service life of an OWT.

The codes of practice currently used to estimate static and cyclic lateral resistances of laterally loaded piles do not effectively address the long-term performance of large diameter piles for two reasons: 1) continuum and time effects of soil are not considered (Rezania *et al*. 2017, Pakar and Bayat 2012a, 2012b) and 2) deformations are not directly related to the number of cycles (Augustesen *et al*. 2000, Hamre *et al*. 2010).

Recently, a number of small-scale tests were conducted to study the effects of repetitive lateral loads on pile deflections (Roesen *et al*. 2013, Klinkvort and Hededal 2014, Chen *et al*. 2015). LeBlanc *et al*. (2010) used small-scale piles (1 g) to examine complex interactions that exist between lateral loads, piles, and soil deposits in order to develop closed form solutions. The tests were performed with loadings typical of foundations for OWTs.

Nevertheless, inability of the most widely used experiments, i.e., 1 g tests, to account for stress distribution under full-scale conditions is well understood. To account for, Truong *et al*. (2019) carried out centrifuge tests varying cyclic load, magnitude ratios and cyclic load sequence in order to gain an insight into the development of net stress, bending moments and deflections as cyclic loading progresses. The soil-pile stiffness degradation and recovery during intermittent episodes of cyclic and subsequent reconsolidation in soft clay have also been investigated in Lai *et al*. (2020) in relation to the mechanism of evolution of cumulative displacement and their consequences to the natural frequency.

However, despite the abundance of studies of soil-pile interaction under repeated lateral loading (Prakash 1962, Davisson 1970, Briaud *et al*. 1983, Lin and Liao 1999, LeBlanc *et al*. 2010, Klinkvort and Hededal 2012, Ibsen *et al*. 2014, Kim *et al*. 2015, Barari *et al*. 2015 and 2017, Truong *et al*. 2019, Klinkvort *et al*. 2018, Yang *et al*. 2018, Chong *et al*. 2019, Lai *et al*. 2020), local aspects of soil-monopile interaction near the pile head under a variety of conditions (i.e., drained, partially drained, or undrained) have not been thoroughly studied.

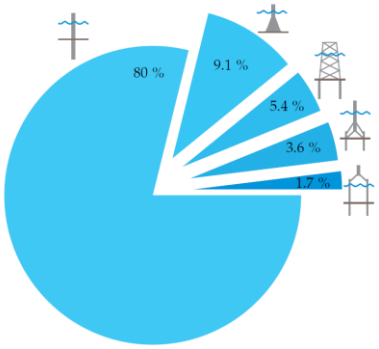

Fig. 1 Distribution of foundation concepts for European offshore wind turbines (EWEA 2016)

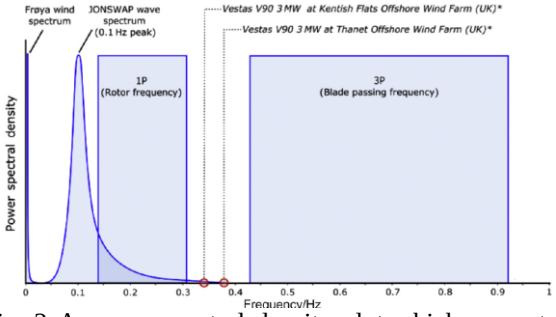

Fig. 2 A power spectral density plot which presents the forcing frequency distribution for a typical three-bladed Vestas V90 3 MW OWT (Lopez-Querol *et al*. 2017)

Large diameter piles support larger wind turbines in shallow to medium-deep waters. Since these piles are exposed to large magnitude lateral loads, it is vital that the long-term performance of these dynamically sensitive structures is better understood. This is particularly relevant to ensure their structural integrity and to control satisfaction departure of overall system dynamics requirements from a design perspective. This paper presents the results from a series of three-dimensional (3D) finite element (FE) analysis to firstly propose an approach to identify the active length of a typical monopile, above which the stiffness of the pile head becomes independent of L and thereby not influencing the target natural frequency. Secondly, this study describes the long-term behavior of OWP monopile foundations that are subjected to lateral oscillations. For the analysis, a multi-surface, plasticity-based constitutive law is used. This model improves some aspects of the current design practices which consider general assumptions that are of limited accuracy regarding the global behavior of SSI. This is achieved by taking into account the effect of cyclic loading according to the number, direction, and magnitude of the load cycles, as well as drainage condition.

2. Design concepts

First, we will provide a brief overview of several published models which served as the basis for our selection of a suitable model to simulate a monopile under cyclic lateral loading. Our main criterion was that the model

would effectively capture the main features of soil-pile interaction behavior under cyclic loading with a minimal number of parameters.

2.1 Existing models

To date, conventional methods of analysis are primarily based on the use of a strain-wedge model (SWM) which assumes that linear horizontal displacement develops along pile length, and this is directly described by mobilization of passive earth pressure in front of the pile. A modified SWM was subsequently adopted by Norris (1986) based on the nonlinear behavior of bedding resistance observed in static triaxial tests. Semi-empirical approaches with explicit integration have also been used. These approaches include accumulation of plastic strain according to an extended wedge model which employs an adjustment factor, a, an empirical coefficient which can be derived from a cyclic triaxial test

$$\left(\varepsilon_{pl,N-1}\right)_i = \left(\varepsilon_{pl,N=1}\right)_i .(N-1)^a \quad (1)$$

Based on tests conducted with piles in cohesionless soil, Kagawa and Kraft (1980) suggest that lateral strains that are concentrated within soil deposits may be approximated by $0.4y/D$, where y represents lateral displacement and D is pile diameter. Furthermore, when Little and Briaud (1988) applied 20 cycles of lateral loading to examine the effect of number of load cycles on cyclic p-y curves, the resulting cyclic excitation was found to influence the mobilized subgrade reaction (P_N).

A corrected form of p-y curves as a function of cycle (N) and increased abscissa (y) values was recently proposed as follows, where y increases exponentially (Peralta and Achmus 2010)

$$y_N = y_1 . N^{\alpha} \quad (2)$$

3. Load transfer analysis based on limiting pile head stiffness

3.1 Validation of a numerical model

Given the complexity of a dynamic soil-foundation interaction system under general loading conditions, it was necessary to validate FE model against experimental data. Hence, comparisons were made against horizontal displacements measured in centrifuge model tests carried out at the Laboratoire Central des Ponts et Chaussées (Rosquoët *et al*. 2004). The centrifuge models were scaled by a ratio of 1/40 and the pile head was loaded with three different force-time histories. Furthermore, different aspects of the one-way cyclic lateral loadings were numerically modeled by using a strain-hardening soil model described by Barari *et al*. (2017) to quantify associated dilation at the soil-foundation interface. A convergence study has also been conducted to determine the sufficient domain size and mesh fineness. Further, the FE predicted force-displacement curve at the pile head is compared with centrifuge

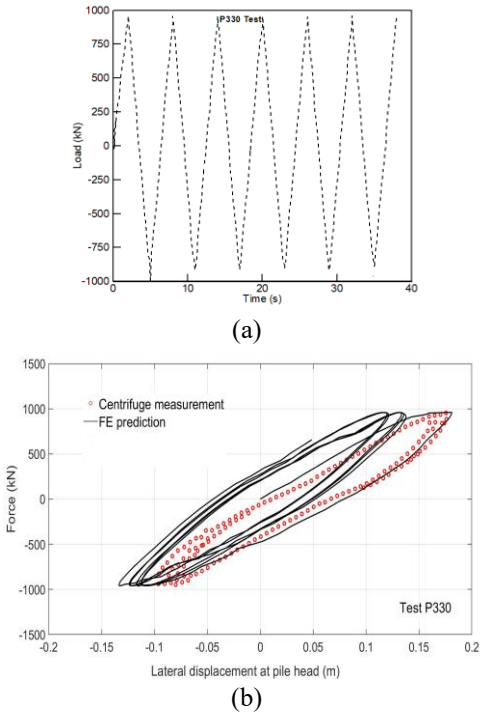

Fig. 3 (a) Load time history of the P330 and (b) Numerically computed and experimentally measured force-displacement curves at pile head in P330 event

experimental measurement in Fig. 3(a) during P330 two-way cyclic loading test with maximum horizontal force 960 kN and minimum horizontal force -960 kN. Cyclic lateral load was applied at 1.6 m above the soil surface, 1 m below the head of the pile model with an embedded length of 12 m in dense sand. Table 1 provides a summary of the calibrated model parameters for the dense soil deposit used in the centrifuge experiment.

The FE result in Fig. 3(b) shows good agreement with the centrifuge test, though it can be seen that it was difficult to rigorously capture the minimum deformations in the FEM, likely due to the installation effect.

3.2 Constitutive model

The accuracy and reliability of FEM analysis is significantly dependent on the appropriateness of the constitutive model used (Rezania *et al*. 2014, 2018, Hendriyawan *et al*. 2019). A constitutive model within the framework of multi-surface plasticity (Prevost 1985) is used here to account for cyclic mobility that contributes to SSI. The model was originally proposed to study the behavior of frictional cohensionless soils. In principle, this constitutive model is an extension of an original multi-surface plasticity concept, with flow and hardening rules (Para 1996, Yang 2000) incorporated. The model has been implemented into OpenSees software (Yang 2000), and its particular advantage is that it accounts for the accumulation of irreversible cycle-by-cycle shear strain, especially in clean medium-to-dense sands.

As illustrated in the stress space shown in Fig. 4, a number of conical yield surfaces are employed in which the

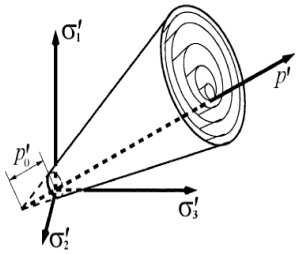

(a)

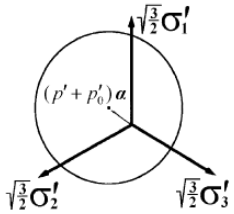

(b)

Fig. 4 (a) Yield envelopes in principal stress space (p': mean effective stress) and (b) Yield envelope in the deviatoric plane (α: kinematic deviatoric tensor representing yield surface coordinates)

uppermost surface is the envelope of peak shear strength. However, in the yield function, f is defined as follows

$$f = \frac{3}{2}(s - p_a\alpha) : (s - p_a\alpha) - M^2 p_a^2 = 0 \quad (3)$$

where $s=\sigma - p\delta$ corresponds to the deviatoric stress tensor. In addition, p_a is defined as the difference between p and a, which represent effective mean normal stress and residual shear strength values, respectively. The other parameters of the formulation include the kinematic deviatoric tensor, α, and M as a material parameter which is represented as a function of the soil friction angle, ϕ.

The multi-surface model which is implemented in OpenSees (Yang 2000, Yang *et al*. 2003, Elgamal *et al*. 2003) incorporates shear-induced contraction and dilation features through a non-associate flow rule. This framework was previously shown to consistently capture hysteretic responses in laterally loaded large slender piles (Barari *et al*. 2017). As shown in Fig. 5, flow rule is defined separately for stress states that are positioned within or beyond the phase transformation (PT) surface. The plasticity framework also adopts a non-associative flow rule which is typically restricted to the volumetric component P'' of the plastic strains, with shear-induced contraction/dilation effects (Fig. 5, phases 2-3) formulated as follows (Parra 1996)

$$P'' = \frac{1-(\eta/\tilde{\eta})^2}{1+(\eta/\tilde{\eta})^2} c_1 \quad \text{(contraction)} \quad (4)$$

$$P'' = \frac{1-(\eta/\tilde{\eta})^2}{1+(\eta/\tilde{\eta})^2} d_1 \exp(d_2\gamma_d) \quad \text{(dilation)} \quad (5)$$

where c_1 and γ_d are scalar coefficients (Yang 2000) which model the rate of contraction and pore-pressure buildup and octahedral shear strain which accumulates over the dilation phase, respectively. In addition, d_1 and d_2,

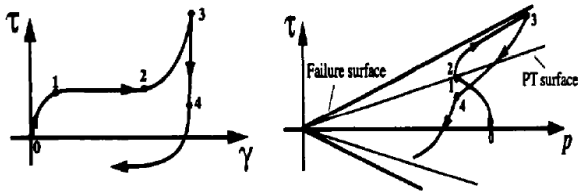

Fig. 5 A typical shear stress-strain response and corresponding effective stress path (Para 1996, Yang 2000)

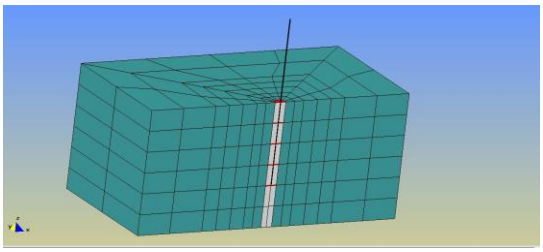

Fig. 6 Representation of the 3D FE mesh discretization

represent rates of volume increase (Yang *et al*. 2003, Elgamal *et al*. 2010), while the effective stress ratio is defined by $(\eta/\tilde{\eta})$, with $\tilde{\eta}$ tracking the stress ratio of the PT surface.

This new framework additionally has the capacity to predict the accumulation of perfectly plastic strain (Fig. 4, phase 1-2), which is often accompanied by a minor change in shear stress.

3.3 FE model, mesh generation, and boundary conditions

Fig. 6 depicts a typical axisymmetric FE model created for 3D analyses of a monopile foundation with a 5 m diameter (D), an embedded length (L) of 30 m, and a thickness (t) of 0.07 m. The radial extent and depth of the soil domain were defined at a distance nearly 1.5 times the embedded length in order to avoid possible constraining effects of the model's boundaries. The discretized model area also had a radius at least ten times the diameter of the foundation, and it consisted of 360 eight-node brick elements and 511 surrounding nodes to model the soil medium. All of the nodes located in the base of the model and lateral boundaries were fixed in all three-directions, while the nodes located in the symmetry plane were fixed against translation in the y direction. Furthermore, eight-node brick elements from the OpenSees library were selected for discretization of the soil medium, and each node had three translational degrees of freedom. The soil-pile interface was assumed to have fully rough contact, with no separation allowed in the normal direction. Non-linear effective stress analyses were performed after assigning the abovementioned constitutive model to the soil elements to account for the nonlinear cyclic response of the geomaterials. Additionally, the pile structure was simulated by using beam-column elements with six degrees of freedom to account for both translational and rocking deformations. The response of the pile structure was modeled with a 3D linear elastic constitutive model.

Table 1 Calibrated model parameters as well as material parameters used to model medium-dense sand

Parameters	Dense sand	medium-dense sand
Saturated mass density (kN / m^3)	19	19
Low strain shear modulous, G_r (MPa)	60	27
Friction angle, ϕ (degree)	41.8	33
Permeability, K (m/s)	6.65×10^{-5}	6.05×10^{-5}
Contraction parameter, c_1	0.05	0.065
PT angle, ϕ_{PT} (degree)	30	23
Dilation parameter d_1	0.8	0.4
Dilation parameter d_2	5	5
Liquefaction parameter 2	-	0.01
Liquefaction parameter 3	-	1

3.4 Solution procedure

A time-domain numerical solution was employed for a dynamic equilibrium formulation of the total soil-foundation system as follows

$$M\ddot{U} + CU + K\dot{U} = R(t) \tag{6}$$

where $\ddot{U}, \dot{U}$ and U are relative nodal acceleration, velocity, and displacement values, respectively. Meanwhile, M, C, and K represent mass, damping, and stiffness matrices, respectively, and $R(t)$ is a time-varying external load. Material damping was considered to be hysteretic in nature and encompassed by an elasto-plastic soil model. Furthermore, effects from both material damping and radiation damping are addressed by [C], a global damping matrix.

By neglecting the relative velocity of the fluid phase in a fully coupled analysis, the FE governing equations in a u-p formulation are as follows

$$\begin{aligned} M\ddot{U} + \int B^T \sigma' dV - QP - f^{(s)} = 0 \\ Q^T \dot{U} + HP + S\dot{P} - f^{(p)} = 0 \end{aligned} \tag{7}$$

where M, B, and $\acute{\sigma}$ represent the mass matrix, strain-displacement matrix, and effective stress vector, respectively; Q corresponds to the discrete gradient operator coupling the solid and fluid phases; P is the pore water pressure vector; H is the permeability matrix; and S is the compressibility matrix. In addition, the effects arising from body forces and the boundary conditions for both solid and fluid phases are represented by f^s and f^p, respectively.

The FE simulations were executed in a stepwise manner. Thus, the initial stress state was generated under gravitational static loading of only the soil elements. Next, the monopile was generated by replacing the soil elements located at the pile location with an elastic isotropic material consisting of 53 six-degrees of freedom beam-column elements with 150 equal degrees of freedom (equalDOF) constraints to connect the structural nodes to the soil nodes at the soil-structure boundaries. Finally, the horizontal loads resulting from wind and wave loads were applied incrementally. The analyses subsequently performed also included parabolic variations of soil modulus with depth

3.5 *Rayleigh damping*

Rayleigh damping was included in the soil-structure model created. A global dynamic equilibrium matrix formulation was written in the following form to generate a damping matrix

$$C = a_0 M + a_1 K \tag{8}$$

where C is the viscous damping matrix which accounts for the independent small strain frequency damping associated with the stress-strain response of cohesionless soils (Chopra 2007), M is the mass matrix, and K is the initial stiffness matrix.

Two non-dimensional coefficients corresponding to mass and stiffness matrices were determined by using two frequencies, f_1 and f_2, and their corresponding damping ratios, ξ_1 and ξ_2, respectively in each case.

$$a_0 = \frac{2\xi\omega_1\omega_2}{\omega_1 + \omega_2} \tag{9a}$$

$$a_1 = \frac{2\xi}{\omega_1 + \omega_2} \tag{9b}$$

Here, $\xi_1 = \zeta_2$ and ω is the circular frequency (rad/s). The damping ratio, ξ, is calculated according to the following equation

$$\xi = \frac{a_0}{4\pi f} + a_1 \pi f \tag{10}$$

where f represents frequency. Two limiting frequencies, f_1= 0.1 and f_2 = 5 Hz, were specified to cover a full range of load frequencies and the natural frequency of the soil-foundation system. In addition, mass and stiffness coefficients were 0.06 and 0.003, respectively; and these resulted in a minimum damping ratio of 5% at the first natural frequency (1.66 Hz).

4. Development of a soil-structure interaction model based on an active length concept

Explicit load-displacement modeling of piled foundations in the lateral direction must be performed in order to better understand lateral load transfer along the length of a pile. The concepts presented here are also important tools for selecting the limiting region for pile length, which must be established prior to performing dynamic analyses. The load-displacement response shown in Fig. 7 corresponds to a monopile with a diameter of 5 m, 0–30 m arm length (h), 20-40 m embedded length under conditions of monotonic loading up to 20 MN, and pile head deflections at seabed level up to 78.5 cm. The soil was modeled as a medium-dense type of sand with material properties similar to the cohesionless geomaterials found in the North Sea (Table 1).

The graphs in Fig. 7 show the pile deflection lines for a 20 MN horizontal load with arm length varied to induce 0, 300, and 600 MNm moments at seabed level. These values are consistent with possible design scenarios for pile

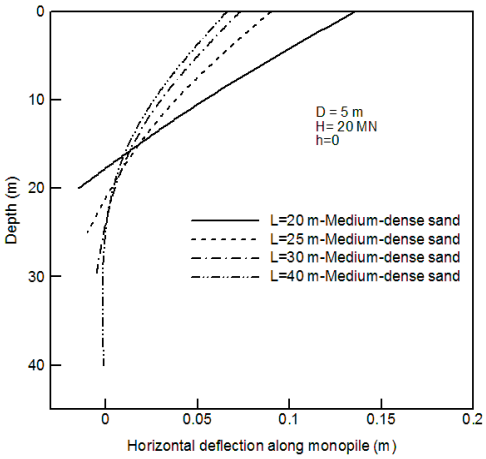

(a)

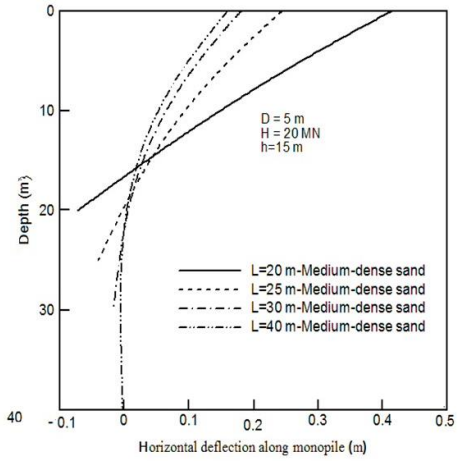

(b)

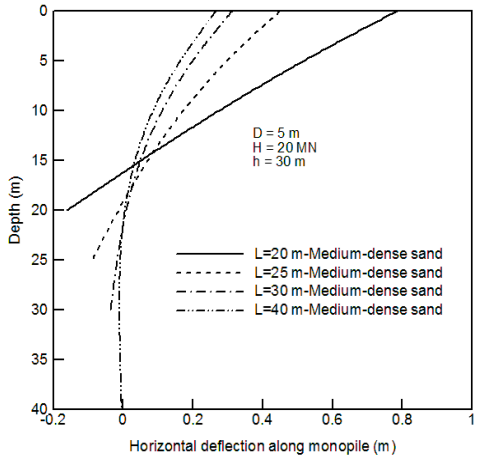

(c)

Fig. 7 Deflection lines for monopiles in medium-dense sand at (a) h=0, (b) h=15 m and (c) h=30 m

exists a limiting region for pile length, referred to as, "active length", along which movements are negligible. As a result, load transfer at the lower part of the pile may be due to compression of the upper region of the pile. However, after a certain pile length, L, the stiffness of the pile head becomes independent of L.

The plots in Fig. 8 show that a critical (i.e., active) length of 25 m for h=0 increases to approximately 30 m for

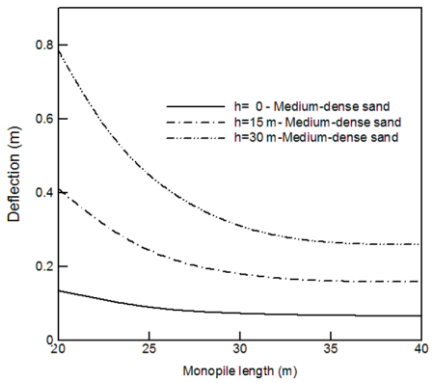

Fig. 8 Dependence of pile head deflection on pile length at 20 MN

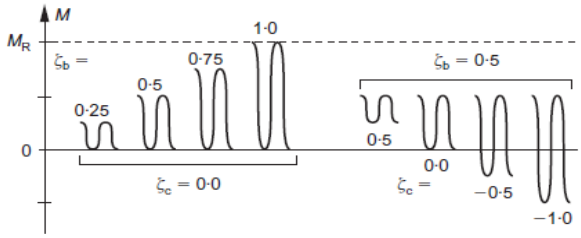

Fig. 9 Characteristics of cyclic loading defined in terms of ξ_b and ξ_c

h=15 m and h=30 m, thereby fulfilling the limitation of head displacement criterion for the serviceability of wind energy plants. Zero-toe-kick criterion can also be elucidated from Fig. 7. In the latter, monopiles at depths less than 30 m exhibit large bending stiffnesses which behave like rigid piles according to Poulos and Davis (1980) and show significant deflection of the pile toe (i.e., “toe kick”). Hence, embedded lengths greater than 30-40 m are necessary to satisfy the zero-toe-kick criterion.

In a subsequent analysis, the performance of a monopile with D=5 m, L=30, and h=15 m was investigated by proposing a number of analytical solutions based on a series of numerical analyses. The analytical solutions linked the evolution of rotation to the number of load cycles, drainage condition as well as to load characteristics.

5. Current methodology: cyclic accumulated strains

This study introduces a methodology based on the results obtained from numerical analyses of monopiles installed in either dry or partially saturated sands under 10,000 lateral load cycles. For consistency, when using the proposed approach for examining the cyclic behavior of a pile with a diameter of D=5 m, the critical length was assumed to be 30 m as determined in the preceding section, since below this depth is considered to be the “active” depth of the pile at which no significant load transfer occurs.

5.1 Definition of load characteristics

Cyclic creep particularly depends on the cyclic stress ratio (CSR), which is defined as

$$\mathrm{CSR} = \frac{(\sigma_1 - \sigma_3)_{\mathrm{cyc}}}{(\sigma_1 - \sigma_3)_{\mathrm{max,stat}}} \tag{11}$$

where $(\sigma_1 - \sigma_3)_{cyc}$ is the cyclic deviator stress and $(\sigma_1 - \sigma_3)_{max,stat}$ is the deviator stress at failure under static condition. The CSR of soil elements in the vicinity of a pile corresponds to a resultant cyclic load ratio (CLR) of the entire soil-pile system, and also represents the ratio of cyclic load amplitude to the static bearing capacity of the monopile. Two non-dimensional parameters, ξ_b, which is practically equal to CLR, and ξ_c, which is introduced hereafter to define load characteristics, are defined as follows

$$\begin{cases} \xi_b = \dfrac{M_{\max}}{M_R} \\ \xi_c = \dfrac{M_{\min}}{M_R} \end{cases} \tag{12}$$

where ξ_b represents the ratio between the maximum load in a load cycle and the static capacity; and ξ_c represents the direction of the lateral load based on the minimum and maximum loads in a cycle (see Fig. 9).

5.2 Static pushover analysis

A series of FE static pushover-type analyses were performed to derive the bearing strength surface of the soil-monopile system in moment (M)-horizontal load (H) space. Based on the results obtained, an envelope was produced (Fig. 10). The results were subsequently normalized with respect to properties of the soil and pile as follows

$$\begin{cases} \bar{M} = \dfrac{M}{DL^3\gamma'} \\ \bar{H} = \dfrac{H}{DL^2\gamma'} \end{cases} \tag{13}$$

$$\bar{\theta} = \sqrt{\frac{P_a}{L\gamma'}}\theta \tag{14}$$

$$\bar{M} = 1.45 - 0.76\bar{H} \tag{15}$$

The monopile was subjected to a monotonically increasing overturning moment until failure occurred. Since M=$H.h$, the interaction between M and H may also be interpreted as the lever arm height that leads to failure for a given H.

5.3 Development of an analytical framework for predicting accumulated deformations

In the next step, values of ξ_b = 0.07, 0.16, 0.27, 0.35, 0.48, and 0.56 were considered for studies of a pile with h=15 m. A laterally loaded rigid pile embedded in cohesionless soil may exhibit hardening behavior, which makes it difficult to determine the failure point in a load-displacement curve. The failure point is taken as the moment at which the pile-head displacement is 0.1D(Cuéllar 2011). Here, the loading eccentricity of the cases was set at e=3D. The FE analyses performed and their loading characteristics are provided in Table 2.

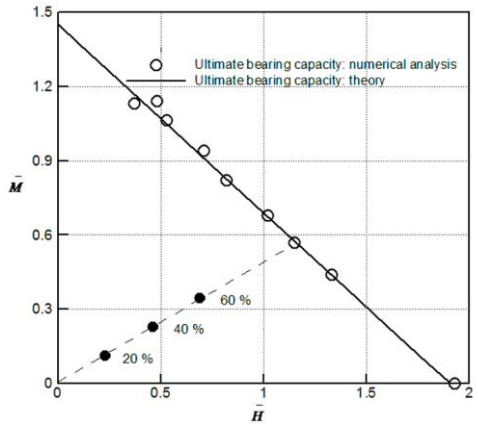

Fig. 10 Range of cyclic loading values in terms of, ξ_b, and in relation to the design loads of a typical OWT

Table 2 Characteristics of the loadings in the FE analyses performed

Load regime	ξ_b	ξ_c	Drainage condition
Model 1	0.07	0	Drained, Partially drained
Model 2	0.27	0	Drained, Partially drained
Model 3	0.35	0	Drained, Partially drained
Model 4	0.48	0	Drained
Model 5	0.56	0	Drained, Partially drained
Model 6	0.27	-0.65	Drained, Partially drained
Model 7	0.27	-0.35	Drained, Partially drained
Model 8	0.27	0.5	Drained, Partially drained
Model 9	0.16	0	Drained

A total of sixteen long-term cyclic loading simulations were initially performed (including nine under drained conditions and seven under partially drained conditions) with 10,000 one-way load cycles ($\xi_c = 0$) applied. If a loading condition is applied such that excess pore pressures do not perfectly dissipate within the period of interest, then a partially drained response is dominant. For a large offshore foundation with a long drainage path, either partially drained or undrained conditions may prevail for months or years depending on excitation characteristics and state parameters. A partially drained condition is not necessarily reflected in design codes in practice (e.g., API 2000, DNV 1992), yet it can exhibit dominant behavior in a soil-foundation system, even when relatively pervious deposits are present.

In the FE simulations performed, the frequency was set at 0.1 Hz. A typical design procedure was followed to ensure the loading ranges were realistic and ξ_b was varied from 0.07 to 0.56. The resulting computed cyclic responses are shown in Figs. 11 and 12 in relation to rotation of the pile, θ, at the soil surface as a function of the number of cycles, N.

The analysis focused on the rotational displacement of the monopile foundation, a relevant consideration in fatigue

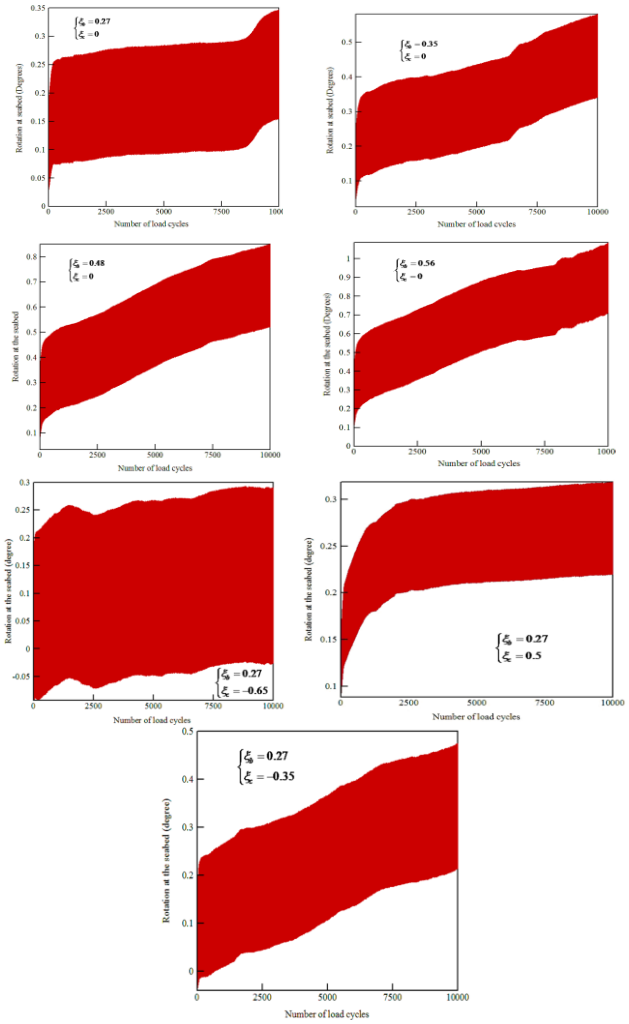

Fig. 11 Computed pile rotation occurs when piles are placed in a dry medium-dense sand and are subjected to sinusoidal loading

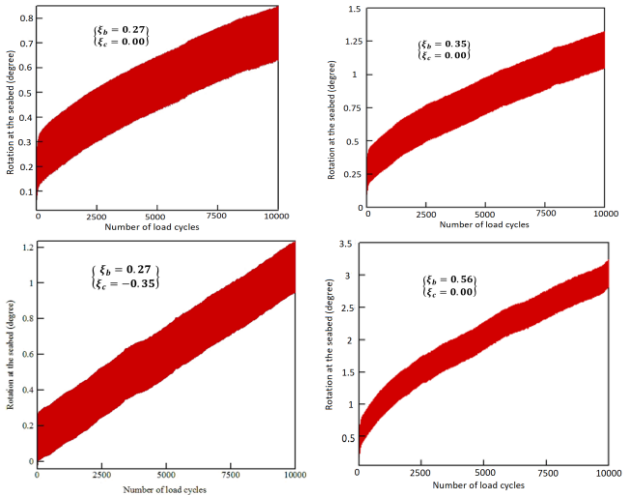

Fig. 12 Computed pile rotation occurs when the pile s are placed in partially drained medium-dense sand and are subjected to sinusoidal loading

design. All of the simulation results were consistent with the presence of a rotation which accumulated in the direction of loading (Figs. 11 and 12).

Meanwhile, the rate effects and pore pressure developments were insignificant over the ranges considered, although different patterns for the accumulated rotation developed at the foundation head level. These results provide a link between soil-structure interaction and sand strain-stress behavior.

In contrast with the API approach (API 2000) which is mainly based on experimental results from tests performed with less than 200 cycles, the lateral cyclic response of the piles examined according to the currently proposed design method were heavily dependent on cyclic load level, load characteristics, number of load repetition, and drainage condition. In addition, evolution of non-slender pile deformations showed a rather stable steady state and energy dissipation per cycle for moderate load level (i.e., $\xi_b = 0.27$) under fully drained conditions. In contrast, under conditions of higher loads in dry sand deposits, and for all of the cases involving saturated sand deposits, the rate of evolution of pile rotation was found to decrease continuously, yet never reached zero. The terminology employed for such behavior is rather diverse from the shakedown behavior proposed by Hettler (1981).

The present findings are consistent with the results of previous triaxial tests performed with cohesionless soils (Helm *et al*. 2000, Festag 2003). Meanwhile, in the present study, an interesting observation was that for a given level, ξ_b, higher magnitudes of ξ_c could lead to lower values of cyclic degradation. Correspondingly, when ξ_c = -0.6, the largest accumulated rotation irrespective of the analysis type performed was observed.

The accumulated rotation paths obtained from our FE analyses are presented in Figs. 13 and 14 with dimensionless terms. Each path moves from an initial zero-load state at a gradient determined by the elastic stiffness, through development of a plastic zone, and then the load states approach an ultimate state. An envelope was subsequently fitted to the numerical data.

The general behavior of the foundation appears to exhibit two trends. In the first part of the curves obtained, rotation accumulates markedly with the number of cycles. Subsequently, the rate of accumulation of permanent rotations tends to diminish (Fig. 13). These results are indicative of system stabilization over thousands of load cycles, under either one-way or two-way loading. While the translational deformations observed in Fig. 13 accumulate slowly over thousands of load cycles, an intermediate meta-stable response was somewhat observed in the saturated analyses, with the rotations accumulating at a moderate rate without stabilization. This pattern is evident in Fig. 14.

The expression that fits these data has the following form

$$\frac{\Delta\theta}{\theta_1} = T_b(\xi_b, R_D)T_c(\xi_c)N^k \tag{16}$$

where $\Delta\theta$ accumulates with rotation evolution during cyclic loading, and this is normalized by the rotation, θ_1, which occurs in the first load cycle. In addition, R_D is indicative of the relative density of the foundation soil. The dimensionless functions in the above formula are interpreted by T_b and T_c in terms of the load

Table 3 Dimensionless functions from different authors used for calibration of Eq.(16) for tests with single foundations

Author	Expressions	K -factor	Dry/Saturated
Zhu *et al*. (2013)	$T_b = \begin{cases} 0 & for \quad \xi_b < 0.23 \\ 0.67\xi_b - 0.16 & for \quad \xi_b \geq 0.23 \end{cases}$ $T_c = \begin{cases} 0.57 + 5.7\xi_c & for \quad \xi_c < -0.7 \\ 1 - \xi_c & for \quad \xi_b \geq -0.7 \end{cases}$	0.39	Dry loose sand
Foglia and Tbscn (2014)	$T_b = 2.41\xi_b^{1.64}$	0.19	Saturated dense sand
Nielsen *et al*. (2017)	$T_b = 1.59\xi_b^2$ $T_c = \begin{cases} 1 - 6\xi_c & for -1 < \quad \xi_c < 0.17 \\ 0 & for \quad 0.17 \leq \xi_c < 1 \end{cases}$	0.39	Saturated dense sand

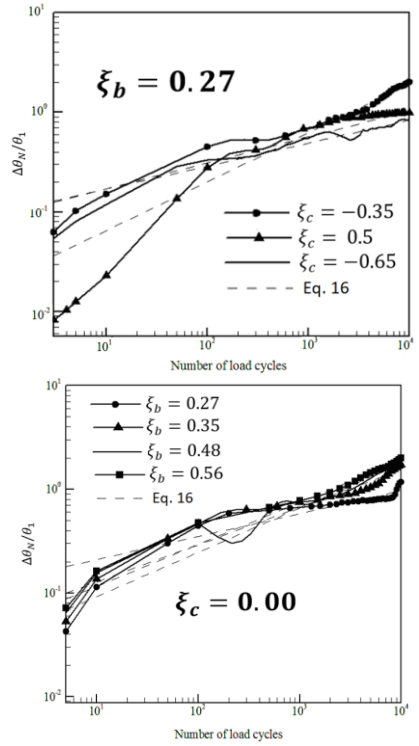

Fig. 13 Normalized accumulated rotation as a function of number of cycles (in a drained analysis). Dotted lines represent Eq. (16)

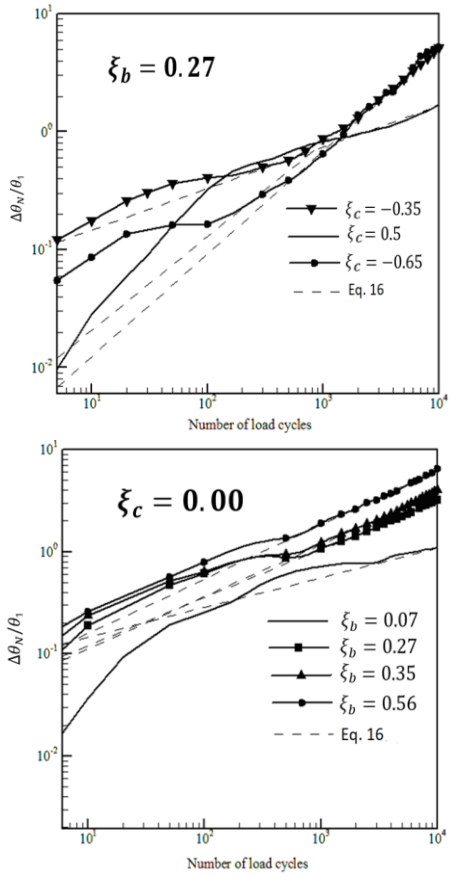

Fig. 14 Normalized accumulated rotation as a function of the number of cycles (in partially drained sand). Dotted lines represent Eq. (16)

characteristics. Consequently, the function, T_c, can be defined here to be equal to unity, which arises from $\xi_c = 0$.

Hence, upon rearrangement of Eq. (16), the normalized form of accumulated rotation is given by

$$\frac{\Delta\theta}{\theta_1} = T_b(\xi_b, R_D)T_c(\xi_c)N^k \longrightarrow \mathrm{k} = \begin{pmatrix} 0.31 & \text{drained} \\ 0.54 & \text{partially drained} \end{pmatrix} \quad (17)$$

The k coefficient identified in regression analyses was found to be dependent on the drainage condition and not the load characteristics. Moreover, for the drained analysis, k is interestingly consistent with the k obtained from previously performed 1g small-scale tests (LeBlanc *et al*. 2010). FE analyses have been shown to be compatible with small-scale physical modeling behavior, and they have also provided key information for improving the modeling and current codes of practice for offshore monopiles. Comparisons of non-dimensional frameworks obtained from FE analyses with frameworks obtained from small-scale physical model tests described in the literature indicate that the latter represents a conservative model for saturated conditions. The reason for this disparity is based on the use of existing empirical expressions which do not account for increased angular rotation of the foundation head if drainage is somewhat prevented (i.e., partial rainage). Moreover, the consequence is remarkable, resulting in an oversight of the effect of soil permeability and development of pore-water pressure in available analytical solutions.

When the above expression is fitted to the data presented in Figs. 13 and 14 (curved lines), values for the T_b function can be empirically derived and they are plotted

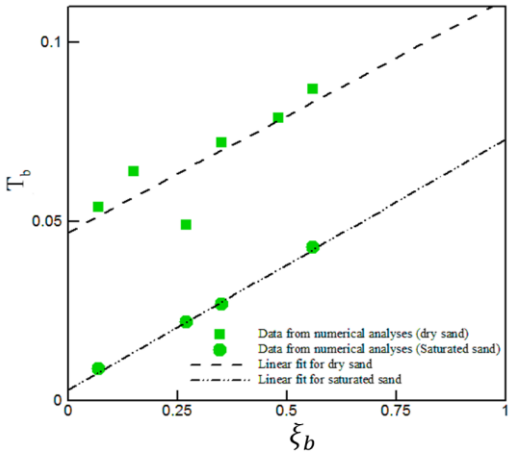

Fig. 15 Fitting parameter, T_b, versus the load characteristic parameter, ξ_b

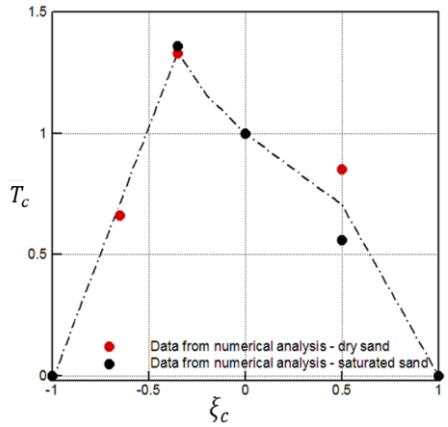

Fig. 16 Fitting parameter, T_c, versus the load characteristic parameter, ξ_c

in Fig. 15 as a function of ξ_b. The influence of relative density is not a focus in the present study. The result obtained arises from the assumption of constant k, which indicates that T_b depends linearly on the magnitude of ξ_b as it varies between 0.07 and 0.56. Of particular interest is the T_c curve shown in Fig. 16. When ξ_c= 1, then T_c must be zero, since no accumulated displacement occurs under static loading. With symmetric loads, as ξ_c= 0, it implies that T_c = 1.

However, the results presented here clearly illustrate that loading with $\xi_c \sim -0.6$ causes an accumulated rotation that is almost 1.5 times larger than that achieved with one-way loading.

To distinguish between the effects of load levels and their characteristics, multiple regression analyses can provide closed form expressions. When this was performed, we immediately observed that the magnitude of the permanent rotations was highly influenced by the mean shear stress level (i.e., load level, ξ_b), while the load direction (equivalent to the load characteristic, ξ_c) was found to contribute to lateral soil resistance mobilization. The latter effect was incorporated into empirical coefficients in a power-law function model.

A closed-form expression for T_b is adopted after fitting

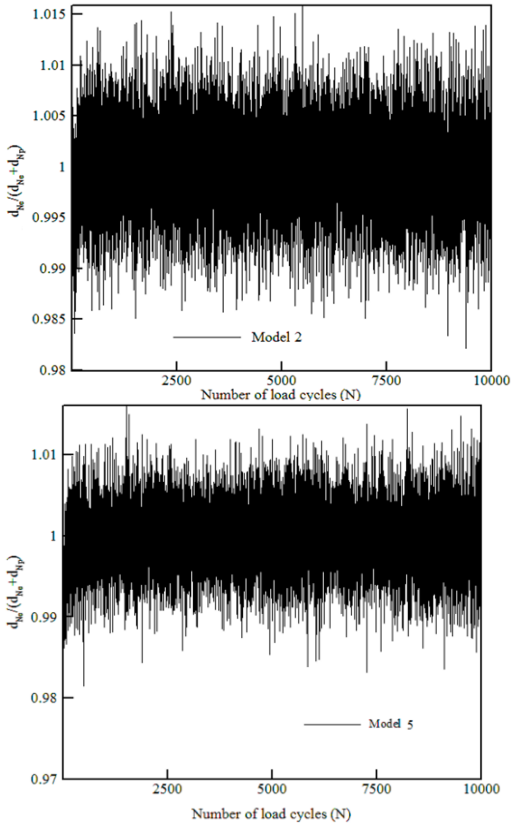

Fig. 17 Ratio of elastic displacement to total displacement in long-term cycling (dry analysis)

a linear line (Fig. 15)

$$T_b = \begin{cases} 0.065\xi_b + 0.047 & \text{dry analysis} \\ 0.07\xi_b + 0.003 & \text{saturated analysis} \end{cases} \quad (18)$$

Incorporating the constraints and fitting two polynomial functions to the data produces the following

$$T_c = \begin{cases} 2.08\zeta_c + 2.06 & \text{for } -1 \le \zeta_c \le -0.35 \\ -0.91\zeta_c^{\,3} + 0.55\zeta_c^{\,2} - 0.63\zeta_c + 1 & \text{for } -0.35 < \zeta_c \le 1 \end{cases} \quad (19)$$

Different authors have calibrated Eq. (16) from physical model tests of single foundations exposed to cyclic loading. The formulation of ζ_b ,ζ_c and α terms are summarized in Table 3.

Previously described model tests have mostly been conducted with a 1 g test set-up and dimensionless equations for scaling the laboratory tests performed. Granular materials may exhibit dilatancy under low stress in 1g tests, and this may lead to an overestimation of the peak friction angle compared to actual conditions in the field. Hence, applicability of findings to large-scale models may not entirely represent environmental conditions (Chen *et al.* 2015).

5.4. Plastic displacements

In this section, a set of analyses is presented which reflects the contribution of elastic displacement, d_e, to total displacement, with the latter consisting of plastic

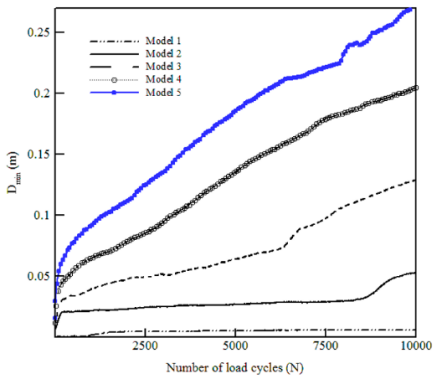

(a)

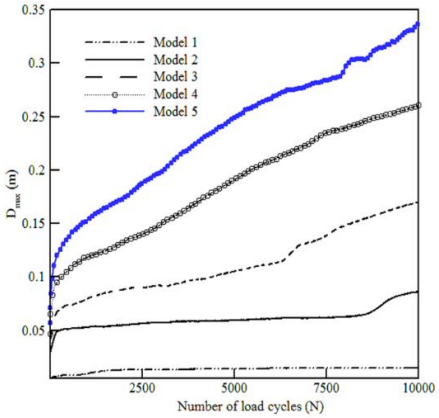

(b)

Fig. 18 Both (a) residual accumulated displacement and (b) peak accumulated displacement were calculated in a dry analysis

displacement, d_p, and elastic displacement, d_e, from a loading cycle ($d_{Ne} + d_{Np}$). Thus, total displacement and elastic displacement of the pile generated in the Nth cycle are given by

$$\left(d_{Np} + d_{Ne}\right) = D_{(N)\max} - D_{(N-1)\min} \tag{20}$$

$$d_{Ne} = D_{(N)\max} - D_{(N)\min} \tag{21}$$

where $D_{(N)\max}$ and $D_{(N)\min}$ represent the peak displacement of a pile in the Nth cycle and residual displacement of the pile after (N-1) cycles, respectively.

The total displacement (d_{Ne} + d_{Np}) in each cycle of models 2 and 5 are also calculated versus the number of cycles. Fig. 17 displays the proportion ratio of the elastic displacement to the total displacement (d_{Ne} / d_{Np} + d_{Ne}). This ratio increases quickly to approximately 97% at the 10th cycle, and approaches 1 at the end of the cycles.

5.5 Residual and peak displacements

In Fig. 18, the residual displacement, $D_{(N)min}$, and the peak displacement, $D_{(N)max}$, of each cycle is presented for the number of cycles, N, for analyses 1–5. The lateral displacement at the 13th cycle in Fig. 18(b) is nearly 25-30% that at the 10,000th cycle, implying that the initial cycles make a significant contribution to pile displacement, $D_{(N)max}$.

6. Impedance functions for a monopile supporting a 8 MW OWT

It is possible to derive wind turbine stiffness from the stiffness of a support structure. However, any alteration that affects the stiffness of the foundation may shift the natural frequency of a soil-foundation system from its design value. This, in turn, could lead to coincidence with forcing excitations. In practice, this is a challenging issue for foundation systems with a soft-stiff design (i.e., the natural frequency of the whole soil-foundation system is set between 1P and 3P), and unplanned resonance may be inevitable.

As interest in wind and wave loading of OWT foundations has grown, it has been realized that static stiffnesses are most appropriately representative of dynamic stiffnesses in a structural analysis context (Laszlo *et al.* 2017). Thus, the aim of this section is to derive a functionally sound, yet practically-oriented, procedure for determining the impedance functions for a laterally-loaded, 5 m diameter monopile. In particular, these functions take into account analysis parameters such as aspect ratio (i.e., the ratio of pile length to pile diameter). Fig. 19 presents a schematic view of a simplified model in which a foundation is replaced by a set of springs characterized by vertical stiffness (K_v), lateral stiffness (K_L), rocking stiffness (K_R), and cross-coupling stiffness (K_{LR}) (Zaaijer 2006).

A few fitted relationships have been described by FE analyses of homogenous and linearly inhomogeneous soils in relation to rigid versus flexible foundation stiffnesses (Randolph 1981, Carter and Kulhawi 1992 and Higgins and Basu 2011). However, little is known about monopile stiffness in inhomogenous soil medium.

In Fig. 20, parabolic soil stiffness variation according to depth is presented. It is observed that Young's modulus of soil increases steadily with depth according to a power law.

Thus, a generalized parabolic form is represented by

$$E_s\left(z\right) = E_{sd}\left[a + \left(1-a\right)z\ /d\right]^n \tag{22}$$

where E_{sd}, a, and n denote Young's modulus of soil at a given depth of pile diameter (z=D) and dimensionless inhomogeneity coefficients, respectively.

When z is set to 0 in Eq. (22), a is given by

$$a = \left(E_{so}\ /\ E_{sd}\right)^{1/n} \tag{23}$$

where E_{s0} accounts for Young's modulus of soil at the surface. The power exponent, n, typically ranges between 0 and 1 to represent over-consolidating to normally consolidated clay, respectively. In the present study, granular soil medium is of particular interest, and it is represented by the exponent value, n = 0.5 (Muir Wood 2004). In addition, stiffness values tabulated in Table 1 are incorporated into Eq. (23).

If the 3D foundation stiffness matrix is reduced to a

Table 4 Flexibility and stiffness coefficients corresponding to various aspect ratios (L_p / D)

Aspect ratio (L_p/D)	$I_L(\frac{m}{GN})$	$I_R(\frac{rad}{GNm})$	$I_{LR}(GN^{-1})$	$k_L(\frac{GN}{m})$	$k_R(\frac{GNm}{rad})$	$k_{LR}(GN)$
4	2.3483	0.024357	-0.179	0.968243	93.3518	-7.1157
5	2.0313	0.021907	-0.1537	1.049387	97.3	-7.36
6	1.928	0.0215	-0.1478	1.0976	98.43	-7.55
8	1.9	0.0214	-0.1475	1.1206	99.3324	-7.686

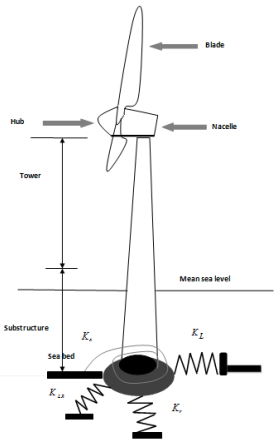

Fig. 19 The OWT model which was adopted to acc ount for impedance functions

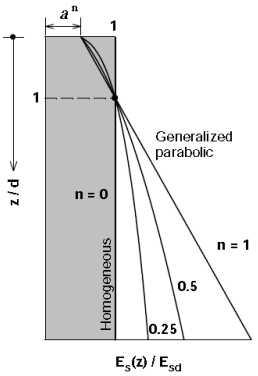

Fig. 20 A schematic view of parabolic soil stiffness variation with depth (n=0.5 in the current study)

two-dimensional matrix by retaining the coordinates 1 and 3 (x-z coordinate), it is presented as

$$\begin{Bmatrix} H \\ M \end{Bmatrix} = \begin{bmatrix} K_L & K_{LR} \\ K_{RL} & K_R \end{bmatrix} \begin{Bmatrix} u_L \\ \theta_R \end{Bmatrix} \tag{24}$$

where H and M denote shear force and over-turning moment, respectively. Moreover, u_L and θ_R represent corresponding deformations as lateral displacement and rotation of the monopile head values, respectively. Accordingly, the behavior of non-slender piles could be expected to be partly dependent on the stiffness of three springs, denoted K_L (lateral spring), K_R (rocking spring), and K_{LR} (cross-coupling spring).

To determine all three unknowns, two of the equations

Table 5 Details of an OWT support structure

Parameters	Values
Top diameter of the tower (m)	3.87
Bottom diameter of the tower (m)	5
Wall thickness of the tower (mm)	27
Height of the tower (m)	90
Platform height (transition piece) (m)	30
Mass of RNA (tons)	451
Mass of Tower (Tons)	413
Rated rotor speed (rpm)	4.8-12.1

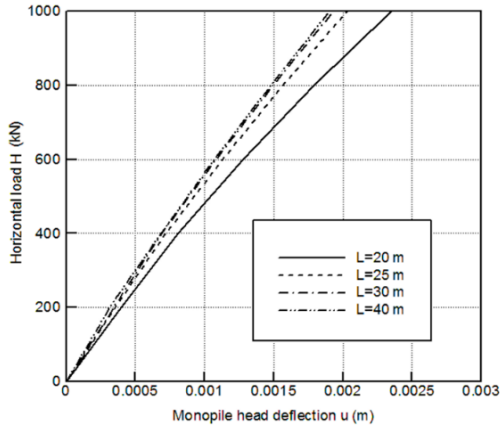

Fig. 21 Monopile head displacement versus applied horizontal load for various aspect ratios

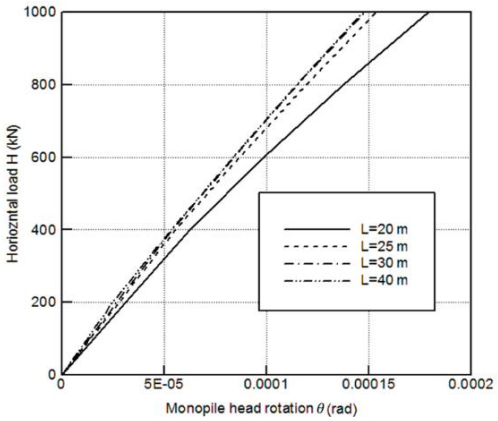

Fig. 22 Resultant monopile head rotation versus acting horizontal load for various aspect ratios

would need to be related via an alternative approach that would require a consideration of flexibility components. Consequently, the inverse of the stiffness matrix has been termed a flexibility matrix, and its components can be readily determined as follows

$$[K]=[I]^{-1} \Rightarrow I = \begin{bmatrix} I_L & I_{LR} \\ I_{LR} & I_R \end{bmatrix}^{-1} = \begin{bmatrix} \frac{u_1}{H_1} & \frac{u_2}{M_2} \\ \frac{\theta_1}{H_1} & \frac{\theta_2}{M_2} \end{bmatrix}^{-1} \tag{25}$$

However, a more practical approach is to relate the

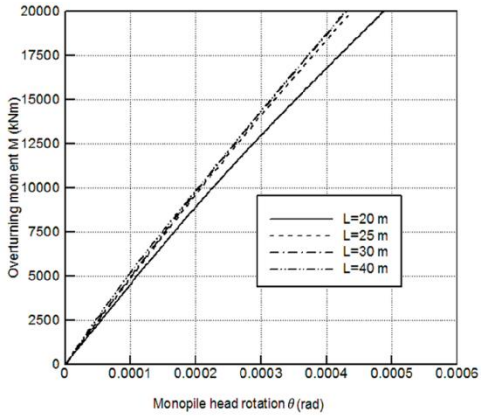

Fig. 23 Resultant monopile head rotation versus acting overturning moment for various aspect ratios

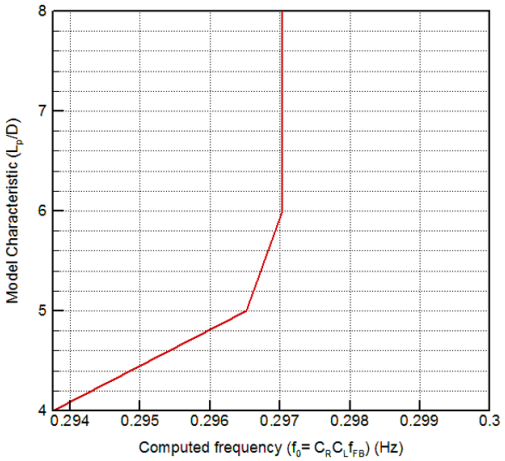

Fig. 24 Predicted natural frequencies of different OWTs have different aspect ratios (L_p/D)

stiffness and flexibility coefficients as

$$K_L = \frac{I_R}{I_L I_R - I^2_{LR}}$$
$$K_R = \frac{I_L}{I_L I_R - I^2_{LR}} \quad (26)$$
$$K_{LR} = \frac{I_{LR}}{I_L I_R - I^2_{LR}}$$

In Figs. 21-23, the results of a series of 3D FE method analyses of monopile head stiffness are presented in which cohesionless medium dense soil was idealized by using a linear elastic medium. In Figs. 21 and 22, evolution of the incipient displacement occurs before all of the monopile models are overturned in force-controlled static push-over FE analyses whose aim is to compute the monopile head flexibility coefficients, I_L and I_{LR}. A flexibility coefficient, I_R, was also included which represents the application of pure bending as a function of moment increases up to 20,000 kN at the foundation head.

The usefulness of this proposed methodology becomes apparent when inverting the slopes of the load-deformation curves to estimate stiffness coefficients according to Eq. (26). In Table 4, the results of using different flexibility and stiffness components for models with different aspect ratios are presented. The models include monopiles ranging from rigid to flexible.

6.1. Computed first natural frequency of a tower-monopile-soil system: An OWT example

We now advance our discussion of the important role of impedance functions described in previous section in relation to assessment of the natural frequency of an OWT.

Currently, dynamic analyses of the whole soil-foundation-tower remain difficult. However, assessment of foundation head stiffness has been shown to be a key component in obtaining authentic estimation of a system's

Eigen frequency. For treatment of the Eigen frequency of this complex system, f_1, the behavior of the surrounding soil, can be governed by what has more recently been termed, *infinite stiffness medium*. In our model, a wind turbine is modeled as an inverted pendulum with flexural rigidity, *EI*, and is characterized by mass properties such as tower mass per meter (m_T) and superstructure mass (m_t) (Vught 2000). Consequently, the first Eigen frequency is described as follows

$$f_1 \cong \sqrt{\frac{3.04EI}{(m_t + 0.227 m_T L_T) 4\pi^2 L^3_T}} \quad (27)$$

where L_T is tower height.

The equation above is consistently challenged by the need to take into account the important aspects of a laterally loaded OWT as accurately as possible. Within the context of soil-foundation interaction, the "1" subscript will hereafter be converted to "FB" for convenience and for consistency with the notation used in the literature.

Characterization of global natural frequency requires consideration of spring stiffness, since the response of OWT depends, to a large extent, on the stiffness of the monopile head and tower bending stiffness. Employing three-spring flexible foundations model proposed by Arany *et al*. (2015) leads to

$$f_0 = C_L C_R f_{FB} \quad (28)$$

where f_0 and f_{FB} are the natural frequency of the entire system and the base frequency that can be approximated from Eq. (27), respectively.

Foundation flexibility factors can be calculated as follows (Bouzid *et al*. 2018):

$$C_R = 1 - \frac{1}{1 + 0.6\left(\eta_R - \frac{\eta^2_{LR}}{\eta_L}\right)} \quad (29)$$

$$C_L = 1 - \frac{1}{1 + 0.5\left(\eta_L - \frac{\eta^2_{LR}}{\eta_R}\right)} \quad (30)$$

$$\eta_L = \frac{K_L L^3}{EI_\eta},\ \eta_{LR} = \frac{K_{LR} L^2}{EI_\eta},\ \eta_L = \frac{K_R L}{EI_\eta} \quad (31)$$

where EI_η is the equivalent tower bending stiffness and η is the soil-foundation interaction coefficient as a function of

tower bending stiffness. It is important to recognize that this new model takes into account interlay interactions of the sub-support structures to provide a better approximation of the actual behavior of the entire system. Furthermore, the value, EI_η, varies throughout a tapered and tubular tower and this is taken into account by using a correction parameter, *f (m)*, which is referred to as a 'tower stiffness coefficient' (Jalbi *et al*. 2018)

$$q = \frac{D_b}{D_T}, \quad f(q) = \frac{1}{3} \times \frac{2q^2(q-1)^3}{2q^2 \ln q - 3q^2 + 4q - 1}$$
$$EI_\eta = EI_{top} \times f(q) \tag{32}$$

where q is determined from the ratio of bottom to top diameter.

To further characterize the proposed framework, a representative 8MW turbine was examined. Table 5 lists the turbine data that were used, and the natural frequency of each OWT model was computed according to Eq. (28) and expressed as an aspect ratio (L_p / D) (Fig. 24). Insights into the effect of soil-structure interaction on an entire system can now be gained from a model in which the natural frequency of the equivalent system is lower that that of the fixed-based structure. As a result, the effect of SSI is shown to reduce the natural frequency of an OWT to a value that is lower than that of the structure under fixed-base conditions. This is particularly relevant for monopiles with a length shorter than their "critical length".

7. Conclusions

In general, geotechnical design is used to obtain a size for offshore foundations, as well as required installation methodologies. For this, different analyses are performed to satisfy design criteria. These should include ULS and SLS analyses. The latter addresses deformation that accumulates due to cyclic loading from various sources (i.e., structural fatigue and storm scenarios) during the life-time of the foundation. Some of these aspects have been indicated above.

Here, 3D axisymmetric dynamic FE modeling of a 5 m diameter monopile foundation was performed with a time domain of up to 10^4 cycles of loading in order to simulate the dynamic properties of the system. Monotonous loading analyses were performed with the maximum moment load ranging from 7-56% of the static capacity. The purpose of these analyses was to evaluate the influence of number of load cycles on the accumulated rocking rotation of a stiff pile at seabed level over long-term cycling. In addition, non-dimensional algebraic formulas for estimating permanent rocking rotation due to variable-amplitude or variable- wind and wave-induced cyclic lateral load characteristics, on stiff piles in medium-dense sand were also presented.

The most important parameters that affected monopile behavior under translational-rocking loads were: load amplitude and characteristics (i.e., embedded length, soil properties, number of cycles, and drainage conditions). In addition, the essential features of the non-dimensional frameworks (i.e., predicted power value given by dry analysis) exhibited good agreement with those measured in existing pile tests in the literature.

Overall, the results from our FE study show that the response of monopiles under combined *M:H* loading is complex. Correspondingly, complex symmetry of T_c values was observed with respect to load characteristics. Within the range of horizontal–moment loads, maximum rotational deformations were found to accumulate in conjunction with negative values of ξ_c. Furthermore, we demonstrated that soil-structure interactions affected the natural frequency of a representative 8 MW wind turbine when monopiles were represented as monopile head springs. Thus, the importance of the proposed methodology is demonstrated, and the main conclusions obtained from this study are summarized as follows:

- Accumulated rotation is directly related to CLR, drainage condition, and number of cycles.
- CLR exerts a significant influence on the cyclic response of a rigid monopile in either dry or saturated sands. In contrast, load direction does not affect pile behavior irrespective of drainage condition.
- Dry analyses (i.e., accumulated deformation underestimation) are less relevant for studies of soil-foundation behaviors relevant to offshore applications.
- To determine the natural frequency of an entire wind turbine system, different assumptions are needed, including those regarding: parabolic variation of soil striffness with depth (i.e., representative of cohesionless soils) and monopile-soil interactions modeled by springs (i.e., K_L, K_{LR}, and K_R). Moreover, comparing the response characteristics of equivalent systems clearly illustrated the decreasing effect of soil-structure interactions. This observation is of paramount importance in the design of OWTs that are installed on monopiles with lengths less than the active depth.

References

Adhikari, S. and Bhattacharya, S. (2011), "Vibrations of wind-turbines considering soil-structure interaction", *Wind Struct.,* **14**(2), 85-112. http://dx.doi.org/10.12989/was.2011.14.2.085.

API (2000), *Recommended Practice for Planning, Designing and Constructing Fixed Offshore Platforms-Working Stress Design*, American Petroleum Institute, Washington, U.S.A.

Arany, L., Bhattacharya, S., Adhikari, S., Hogan, S.J. and MacDonald, J.H.G. (2015), "An analytical model to predict the natural frequency of offshore wind turbines on three-springs flexible foundations using two different beam models", *Soil Dyn. Earthq. Eng.*, **74**, 40-45. https://doi.org/10.1016/j.soildryn.2015.03.007.

Augustesen, A., Sørensen, S., Ibsen, L. and Brødbæk, K. (2000), *Comparison of Calculation Approaches for Monopiles for Offshore Wind Turbines*, Numer. Meth. Geotech. Eng., CRC Press, 901-906.

Barari, A. and Ibsen, L.B. (2017), "Insight into the lateral response of offshore shallow foundations", *Ocean Eng.*, **144**(1), 203-210. https://doi.org/10.1016/j.oceaneng.2017.08.012.

Barari, A. and Ibsen, L.B. (2018), *A Macro-Element Approach for Non-Linear Response of Offshore Skirted Footings*, in *Civil Infrastructures Confronting Severe Weathers and Climate*

Changes Conference, Springer, Cham, Switzerland.

Barari, A., Bagheri, M., Rouainia, M. and Ibsen, L.B. (2017), "Deformation mechanisms of offshore monopile foundations accounting for cyclic mobility effects", *Soil Dyn. Earthq. Eng.*, **97**, 439-453. https://doi.org/10.1016/j.soildyn.2017.03.008.

Barari, A., Bayat, M., Saadati, M., Ibsen, L.B. and Vabbersgaard, L.A. (2015), "Transient analysis of monopile foundations partially embedded in liquefied soil", *Geomech. Eng.*, **8**(2), 257-282. https://doi.org/10.12989/gae.2015.8.2.257.

Bisoi, S. and Haldar, S. (2014), "Dynamic analysis of offshore wind turbine in clay considering soil–monopile–tower interaction", *Soil Dyn. Earthq. Eng.*, **63**, 19-35. https://doi.org/10.1016/j.soildyn.2014.03.006.

Bouzid, D.A., Bhattacharya, S. and Ostmane, L. (2018), "Assessment of natural frequency of installed offshore wind turbines using nonlinear finite element considering soil-monopile interaction", *J. Rock Mech. Geotech. Eng.,* **10**, 333-346. https://doi.org/10.1016/j.jrmge.2017.11.010.

Briaud, J., Smith, T.D. and Meyer, B.J. (1983), "Using the pressuremeter curve to design laterally loaded piles", *Proceedings of the Annual Offshore Technology Conference*, Houston, Texas, U.S.A., May.

Carter, J.P. and Kulhawy, F.H. (1992), "Analysis if laterally loaded shafts in rock", *J. Geotech. Eng.*, **118**(6), 839-855.

Chen, R.P., Sun, Y.X., Zhu, B. and Guo, W.D. (2015), "Lateral cyclic pile-soil interaction studies on a rigid model monopile", *Proc. Inst. Civ. Eng. Geotech. Eng.*, **168**(GE2),120-130. https://doi.org/10.1680/geng.14.00028.

Chong, S.H., Shin, H.S. and Cho, G.C. (2019), "Numerical analysis of offshore monopile during repetitive lateral loading", *Geomech. Eng.*, **19**(1), 79-91. http://dx.doi.org/10.12989/gae.2019.19.1.079.

Chopra, A.K. (2007), *Dynamics of Structures: Theory and Applications to Earthquake Engineering*, Upper Saddle River, New Jersey: Pearson Education Inc.,

Cuéllar, P. (2011), "Pile foundations for offshore wind turbines: Numerical and experimental investigations on the behaviour under short-term and long-term cyclic loading", Ph.D. Dissertation, Technische Universität Berlin, Berlin, Germany.

Davisson, M.T. (1970), *Lateral Load Capacity of Piles*, Highway Research Record, (333).

DNV (1992), *Classification Notes No. 30.4, Foundations*, Det Norske Veritas, Oslo, Norway.

Doherty, P. and Gavin, K. (2012), "Laterally loaded monopile design for offshore wind farms", *Proceedings of the Institution of Civil Engineers: Energy*, **165**(1), 7-17. https://doi.org/10.1680/ener.11.00003.

Elgamal, A., Lu, J. and Forcellini, D. (2010), "Mitigation of liquefaction-induced lateral deformation in a sloping stratum: Three-dimensional numerical simulation", *J. Geotech. Geoenvironment. Eng.*, **135**(11), 1672-1682. https://doi.org/10.1061/(ASCE)GT.1943 5606.0000137.

Elgamal, A., Yang, Z., Parra, E. and Ragheb, A. (2003), "Modeling of cyclic mobility in saturated cohesionless soils", *Int. J. Plast.*, **19**(6), 883-905. https://doi.org/10.1016/S0749-6419(02)00010-4.

EWEA (2016), *The European Offshore Wind Industry-Key Trends and Statistics 2015*.

Festag, G. (2003), *Experimentelle und Numerische Untersuchungen zum Verhalten von Granularen Materialien unter Zyklischer Beanspruchung*, Master Thesis, Technische Universität Darmstadt, Darmstadt, Germany,

Foglia, A. and Ibsen, L.B. (2014). *Monopod Bucket Foundation under Cyclic Lateral Loading,* DCE Technical Report No. 176, Department of Civil Engineering, Aalborg University.

Ghasemi, G., Barari, A. and Choobbasti, A.J. (2014), "Seismic analysis of pile-soil interaction in liquefiable soils via gap elements", *Advan. Soil Dyn. Found. Eng*., 323-332. https://doi.org/10.1061/9780784413425.033.

Hamre, L., Khankandi, S., Strøm, P. and Athanasiu, C. (2010), *Lateral Behaviour of Large Diameter Monopiles at Sheringham Shoal Wind Farm*, in *Frontiers in Offshore Geotechnics II*, CRC Press, 575-580

Helm, J., Laue, J. and Triantafyllidis, T. (2000), "Zur Verformungsentwicklung von Böden unterzyklischer Beanspruchung", *Bautechnik*, **77**(6), 405-415. https://doi.org/10.1002/bate.200003070.

Hendriyawan, H., Primananda, M.A., Puspita, A.D., Guo, C., Hamdhan, I.N., Tahir, M.M., Pham, B.T., Mu'azu, M.A. and Khorami, M. (2019), "Simplification analysis of suction pile using two dimensions finite element modeling", *Geomech. Eng.*, **17**(4), 317-322. https://doi.org/10.12989/gae.2019.17.4.31.

Hettler, A. (1981), *Verschiebungen Starrer und Elastischer Gründungskörper in Sand bei Monotoner und Zyklischer Belastung*, Ph.D. Thesis, University of Karlsruhe, Germany.

Higgins, W. and Basu, D. (2011), *Fourier Finite Element Analysis of Laterally Loaded Piles in Elastic Media*, Internal Geotechnical Report 2011-1. University of Connecticut, U.S.A.
https://doi.org/10.1016/B978-0-12-809451-8.00014-X.

Ibsen, L.B., Asghari, A., Bagheri, M. and Barari, A. (2014), "Response of monopiles in sand subjected to one-way and transient cyclic lateral loading", *Advan. Soil Dyn. Found. Eng.*: 312-322.

Ibsen, L.B., Barari, A. and Larsen, K.A. (2015). "Effect of embedment on the plastic behavior of bucket foundations", *J. Waterway, Port, Coastal Ocean Eng.*, **141**(6), 06015005. https://doi.org/10.1061/(ASCE)WW.1943-5460.0000284.

Ibsen, L.B., Barari, A., Larsen, K.A. (2012), "Modified vertical bearing capacity for circular foundations in sand using reduced friction angle", *Ocean Eng.*, **47**, 1-6. https://doi.org/10.1016/j.oceaneng.2012.03.003.

Jalbi, S., Shadlou, M. and Bhattacharya. (2018), "Impedance functions for rigid skirted caissons supporting offshore wind turbines", *Ocean Eng.*, **150**, 21-35. https://doi.org/10.1016/j.oceaneng.2017.12.040.

Kagawa, T. and Kraft, L.M. (1980), ''Lateral load-deflection relationships of piles subjected to dynamic loadings'', *Soils Found*., **20**(4), 19-34. https://doi.org/10.3208/sandf1972.20.4_19.

Kim, G., Kyung, D., Park, D. and Lee, J. (2015), "CPT-based p-y analysis for mono-piles in sands under static and cyclic loading conditions", *Geomech. Eng.,* **9**(3), 313-328. https://doi.org/10.12989/gae.2015.9.3.313.

Klinkvort, R. and Hededal, O. (2014), ''Effect of load eccentricity and stress level on monopile support for offshore wind turbines'', *Canadian Geotech. J.*, **51**(9), 966-974. https://doi.org/10.1139/cgj-2013-0475.

Klinkvort, R.T., Black, J.A., Bayton, S.M., Haigh, S.K., Madabhushi, G.S.P., Blanc, M., Thorel, L., Zania, V., Bienen, B. and Gaudin, C. (2018), "A review of modelling effects in centrifuge monopile testing in sand", *9th Int. Conference Physical Modeling Geotech., ICPMG*, London, United Kingdom.

Lai, Y., Wang, L., Hong, Y. and He, B. (2020), "Centrifuge modeling of the cyclic lateral behavior of large-diameter behavior of large-diameter monopiles in soft clay: Effects of episodic cycling and reconsolidation", *Ocean Eng.*, **200**, 107048. https://doi.org/10.1016/j.oceaneng.2020.107048.

Larsen, K.A., Ibsen, L.B. and Barari, A. (2013), "Modified expression for the failure criterion of bucket foundations subjected to combined loading", *Canadian Geotech. J.*, **50** (12), 1250-1259. https://doi.org/10.1139/cgj-2012-0308.

Laszlo, A., Bhattacharya, S., Macdonald, J. and Hogan, S.J.

(2017), "Design of monopiles for offshore wind turbines in 10 steps", *Soil Dyn. Earthq. Eng.*, **92**, 126-152. https://doi.org/10.1016/j.soildyn.2016.09.024.

LeBlanc, C., Houlsby, G.T. and Byrne, B.W. (2010), "Response of stiff piles in sand to long-term cyclic lateral loading", *Geotechnique*, **60**(2), 79-90. https://doi.org/10.1680/geot.7.00196.

Lin, S. and Liao, J. (1999), "Permanent strains of piles in sand due to cyclic lateral loads", *J. Geotech. Geoenvironment. Eng.*, **125**(9), 798-802. https://doi.org/10.1061/(ASCE)1090-0241(1999)125:9(798).

Little, R.L. and Briaud, J.L. (1988), *Full Scale Cyclic Lateral Load Tests on Six Single Piles in Sand*, Texas A and M Univ. College Station Dept of Civil Engineering.

Long, J.H. and Vanneste, G. (1994), ''Effects of cyclic lateral loads on piles in sand'', *J. Geotech. Geoenviron. Eng.*, **120**(1), 225-244. https://doi.org/10.1061/(ASCE)0733-9410(1994)120:1(225).

Lopez-Querol, S., Cui, L. and Bhattacharya, S. (2017), "Numerical methods for SSI analysis of offshore wind turbine foundations", *Wind Energy Eng*., 275-297.

Madsen, S., Pinna, R., Randolph, M.F. and Andersen, L.V. (2015), "Buckling of monopod bucket foundations - influence of boundary conditions and soil-structure interaction", *Wind Struct.*, **21**(6), 641-656. https://doi.org/10.12989/was.2015.21.6.641.

Muir Wood, D. (2004), *Geotechnical Modeling*, CRC Press, London, U.K.

Nielsen, S.D., Ibsen, L.B. and Nielsen, B.N. (2017), "Response of cyclic-loaded bucket foundations in saturated dense sand", *J. Geotech. Geoenviron. Eng.*, **143**(11), 04017086. https://doi.org/10.1061/(ASCE)GT.1943-5606.0001787.

Norris, G.M. (1986), "Theoretically based BEF laterally loaded pile analysis", *Proceedings of the 3rd International Conference on Numerical Methods in Offshore Piling*, Nantes, France, 361-386.

Pakar, I. and Bayat, M. (2012a), "Analytical study on the non-linear vibration of Euler-Bernoulli beams", *J. Vibroeng.*, **14**(1), 216-224.

Pakar, I. and Bayat, M. (2012b), "On the approximate analytical solution for parametrically excited nonlinear oscillators", *J. Vibroeng.*, **14**(1), 423-429.

Parra, E. (1996), "Numerical modeling of liquefaction and lateral ground deformation including cyclic mobility and dilative behaviour in soil systems", Ph.D. Dissertation, Rensselaer Polytechnic Institute, New York, U.S.A.

Peralta, P. and Achmus, M. (2010), "An experimental investigation of piles in sand subjected to lateral cyclic loads", *Proceedings of the 7th International Conference on Physical Modelling in Geotechnics (ICPMG2010)*, Zurich, Switzerland.

Poulos, H.G. and Davis, E.H. (1980), *Pile Foundation Analysis and Design*, Wiley, New York, U.S.A.

Prakash, S. (1962), ''Behavior of pile groups subjected to lateral loads'', Ph.D. Dissertation, University of Illinois, Urbana, Chicago, U.S.A.

Prevost, J.H. (1985), "A simple plasticity theory for frictional cohensionless soils", *Soil Dyn. Earthq. Eng.*, **4**(1), 9-17. https://doi.org/10.1016/0261-7277(85)90030-0.

Randolph, M. (1981), "The response of flexible piles to lateral loading", *Geotechnique*, **31**, 247-259. https://doi.org/10.1680/geot.1981.31.2.247.

Rezania, M., Mousavi Nezhad, M., Zanganeh, H., Castro, J. and Sivasithamparam, N. (2017), "Modeling pile setup in natural clay deposit considering soil anisotropy, structure, and creep effects: Case study", *Int. J. Geomech.*, **17**(3), 04016075. https://doi.org/10.1061/(ASCE)GM.1943-5622.0000774.

Rezania, M., Nguyen, H., Zanganeh, H. and Taiebat, M. (2018), "Numerical analysis of Ballina test embankment on a soft structured clay foundation", *Comput. Geotech.*, **93**, 61-74. https://doi.org/10.1016/j.compgeo.2017.05.013.

Rezania, M., Sivasithamparam, N. and Mousavi Nezhad, M. (2014), "On the stress update algorithm of an advanced critical state elasto-plastic model and the effect of yield function equation", *Fin. Elements Anal. Des*., **90**, 74-83. https://doi.org/10.1016/j.finel.2014.06.009.

Roesen, H.R., Ibsen, L.B. and Andersen, L.V. (2013), ''Experimental testing of monopiles in sand subjected to one-way and long-term cyclic lateral loading'', *Proceedings of the 18th International Conference on Soil Mechanics and Geotechnical Engineering*, Paris, France, September.

Rosquoët, F., Garnier, J., Thorel, L. and Canepa, Y. (2004), *Horizontal Cyclic Loading of Piles Installed in Sand: Study of the Pile Head Displacement and Maximum Bending Moment*, in *Cyclic behaviour Soils Liquefaction Phenomena*, 363-368.

Truong, P., Lehane, B.M., Zania, V. and Klinkvort, R.T. (2019), "Empirical approach based on centrifuge testing for cyclic deformations of laterally loaded piles in sand", *Geotechnique*, **69**(2), 133-145. https://doi.org/10.1680/jgeot.17.P.203.

Vught, J.H. (2000), "Considerations on the dynamics of support structures for an offshore wind energy converter", Ph.D. Dissertation, Delft University of Technology, Delft, The Netherlands.

Wang, X., Zeng, X., Li, J. and Yang, X. (2018), "Lateral bearing capacity of hybrid monopile-friction wheel foundation for offshore wind turbines by centrifuge modeling", *Ocean Eng.*, **148**, 182-192. https://doi.org/10.1016/j.oceaneng.2017.11.036.

Yang, X., Zeng, X., Wang, X. and Yu, H. (2018), "Performance of monopile-friction wheel foundations under lateral loading for offshore wind turbines", *Appl. Ocean Res.*, **78**, 14-24. https://doi.org/10.1016/j.apor.2018.06.005.

Yang, Z. (2000), *Numerical Modeling of Earthquake Site Response Including Dilation and Liquefaction*, Ph.D. Dissertation, Columbia University, New York, U.S.A.

Yang, Z., Elgamal, A. and Parra, E. (2003), "A computational model for cyclic mobility and associated shear deformation", *J. Geotech. Geoenviron. Eng.*, **129**(12), 1119-1127. https://doi.org/10.1061/(ASCE)1090-0241(2003)129:12(1119).

Youn, H. and Bouassida, M. (2018), *New Prospects in Geotechnical Engineering Aspects of Civil Infrastructures*, Sustainable Civil Infrastructures. Springer.

Zaaijer, M.B. (2006), "Foundation modeling to assess dynamic behaviour of offshore wind turbines", *Appl. Ocean Res.*, **28**(1), 45-57. https://doi.org/10.1016/j.apor.2006.03.004.

Zhu, B., Byrne, B.W. and Houlsby, G.T. (2013), "Long-term lateral cyclic response of suction caisson foundations in sand", *J. Geotech. Geoenviron. Eng*., **139**(1). https://doi.org/10.1061/(ASCE)GT.1943-5606.0000738.

CC